The three-phase contact line shape and eccentricity effect of anisotropic wetting on hydrophobic surfaces

Kashaninejad, Navid; Nguyen, Nam-Trung; Chan, Weng Kong

2013

Kashaninejad, N., Nguyen, N. T., & Chan, W. K. (2013). The three-phase contact line shape and eccentricity effect of anisotropic wetting on hydrophobic surfaces. Soft Matter, 9, 527-535.

https://hdl.handle.net/10356/95354

https://doi.org/10.1039/C2SM26963E

Soft Matter

Cite this: DOI: 10.1039/c2sm26963e

www.rsc.org/softmatter

PAPER

The three-phase contact line shape and eccentricity effect of anisotropic wetting on hydrophobic surfaces

Navid Kashaninejad, Nam-Trung Nguyen* and Weng Kong Chan

Received 24th August 2012, Accepted 16th October 2012
DOI: 10.1039/c2sm26963e

This paper experimentally evaluates the combined effects of eccentricity, relative spacing, and viewing directions on the wetting conditions and the three-phase contact line shapes of hydrophobic surfaces patterned with discrete micropillars. Different techniques to depict the tortuosity of the contact line between the water droplet and microstructured surfaces are presented. First, square micropillars with different values of normalized eccentricity, ε^*, and relative spacing, D^*, were fabricated using a double casting replication technique. Subsequently, the contact angles were measured along different viewing angles by gradually rotating the sample from 0° to 180°. The contact angle distribution was found as a periodic function of the viewing angle whose period depends on the micropillar eccentricity. The results showed that anisotropy increases by increasing the micropillar eccentricity or decreasing the pillar relative spacing. However, the effect of changing the micropillar eccentricity was much more pronounced. Micropillars with $\varepsilon^* = 0.75$ and smaller D^* showed maximum degrees of anisotropic wetting and droplet distortion corresponding to 7% and 15%, respectively. Using the measured droplet aspect ratio, corrugated shapes of the three-phase contact line of the micropillars were also reconstructed. Finally, a simple yet effective semi-analytical model, based on Fourier series curve-fitting of the experimental data, was developed to describe the equilibrium 3D shape of the droplet on anisotropic surfaces. Experimental and simulation results reveal that the degrees of anisotropic wetting and droplet distortion were directly proportional to the energy barriers of the system, resulting from the noncircular corrugated shape of the three-phase contact line. The obtained results may further shed light on the underlying mechanism influencing anisotropic wetting on micropatterned surfaces.

Introduction

Controlling the wetting behavior of a droplet on a solid surface is of critical importance owing to its wide range of applications including surface coating, surface tension driven flow and liquid transport in emerging areas such as micro/nanofluidics, biomedical devices, biomimetics, and digital microfluidics. Wettability is quantified by the contact angle which macroscopically manifests the intermolecular interactions at the three-phase contact line. In contrast to isotropic surfaces, the contact angle varies along different viewing angles on anisotropic surfaces. Directional dependency of the contact angle known as anisotropic wetting is prevalent in nature such as allowing water droplet movement along the edge of rice, pandanus (screwpine) and bamboo leaves,[1–3] and rolling off (pinning) of a drop along (against) the radial outward direction of the central axis of the butterfly wings.[4] In general, asymmetry of either surface chemistry or surface morphology may lead to directional dependency of the contact angle. Accordingly, two methods can be devised to artificially fabricate anisotropic surfaces, namely one-dimensional (1D) and two/three-dimensional (2D/3D) methods. In the 1D approach, periodic planar regions of alternating hydrophobic and hydrophilic strips are formed using chemical coatings on macroscopically smooth surfaces. The wettability of these surfaces was analyzed experimentally, theoretically and numerically through the literature.[5–11] In the 2D/3D approach, rough surfaces with asymmetrical micro/nano-protrusions are fabricated as a result of highly advanced micro/nano-fabrication techniques.

Because of its potential applications, attempts to identify the roles of key parameters influencing the anisotropic wetting are of great interest for the research community. Directional dependency of the contact angle of different ranges of natural surfaces, such as rice leaf structures,[12] and other synthetic microstructures, including checkerboard-patterned surfaces,[13] wrinkled surfaces,[14,15] ratchet-like topographical structures,[16] elliptical silicon arrays[17] and stooped polymer nanohairs,[18] and tilted polymer nanorod arrays,[26] has been evaluated. Among many asymmetric microstructures, surfaces with periodic parallel grooves at different length scales, pitches, heights, *etc.* were extensively investigated in the literature.[19–34] Chen *et al.*[20]

School of Mechanical and Aerospace Engineering, Nanyang Technological University, Singapore 639798. E-mail: mntnguyen@ntu.edu.sg; Fax: +65 6791 1859; Tel: +65 6790 4457

reported a semi-analytical and an experimental study of micro-groove surfaces. Higher observable contact angle in the front view of the droplet compared to the side view was attributed to the squeezing and pinning of the droplet along the direction of the grooves and stretching across that direction. Neuhaus *et al.*[34] investigated microstructured surfaces consisting of both groove and square pillars with three different wetting conditions, namely hydrophobic, moderately hydrophilic and very hydrophilic. They found that on a moderately hydrophilic groove substrate, a water droplet pinned to the structure and became elongated. The contact angle was considerably higher (up to 37°) along the viewing direction parallel to the groove as compared to that from the perpendicular direction. In the case of square micropatterns, a droplet shape deviated from being circular especially for the case of moderate hydrophilicity, and interestingly anisotropy was observed on those topographically symmetric structures. The contact angle was higher (around 4° for the case of hydrophobic and 9° for the case of moderately hydrophilic conditions) along the edge as compared to the diagonal viewing direction of the square pillars. For both patterns in the hydrophilic state, almost the same isotropic contact angle was reported. Long *et al.*[29] systematically investigated the static and dynamic wetting anisotropies of eight different translationally symmetric elongated ridges by gradually increasing the length of the subsequent discrete ridge to finally form a continuous microridge structure. They reported that by splitting the continuous ridges into the discrete ones, the static and dynamic contact angle anisotropies substantially decreased but did not disappear.

Recently, we introduced another important geometrical parameter of the microstructured surfaces termed as eccentricity, ε, centre-to-centre offset distance between successive columns of a square lattice of micropillars.[35] This parameter quantifies how much the micropatterned surface deviates from being symmetric and is shown schematically in Fig. 1(a). As reported previously, increasing the values of the micropillar eccentricity not only makes the surface asymmetric but also increases the contact angle hysteresis.[35] The increase in contact angle hysteresis emphasises the importance of the line tension, an additional term in the Gibbs free energy, as a result of the distortions of the three-phase contact line. The distorted nature of the contact line on eccentricity-induced asymmetric micropillars implies that the contact angle may become different along different viewing angles, as opposed to the non-distorted circular shapes of the contact line on isentropic surfaces. Thus, changing the eccentricity may lead to contact angle anisotropy. However, depicting the microscopic tortuosity of the three-phase contact line of a sessile water droplet on microstructured surfaces is a challenging problem. Alternative methods to depict the contact line shapes of non-aqueous fluids use either the microscopic images of molten Woods after solidification[36] or SEM images of non-volatile organic liquids.[31] In this paper, we address this issue by systematically measuring the contact angles, widths, and heights at different viewing directions, and schematically depict the water droplet three-phase contact lines using two-dimensional and three-dimensional methods. Additionally, this paper investigates the directional dependency of the contact angle as a function of eccentricity at different micropillar relative spacing. Wetting anisotropy of the micropillar surfaces is quantified by introducing two new parameters, degree of anisotropic wetting and degree of anisotropic drop distortion. The effect of changing the micropillar eccentricity and spacing on these parameters is investigated and discussed. The results of the present paper can further elucidate the effect of the three-phase contact line of the micropillars, in terms of the micropillar eccentricity, and provide additional insight into further investigations to modify the existing wetting theories.

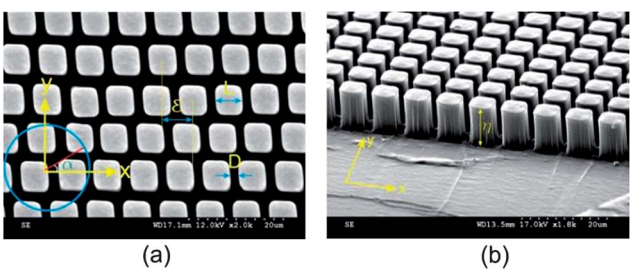

Fig. 1 Representative SEM images of the fabricated pillars: (a) top view of the micropillars with coordinates and geometrical parameters used in this study. (b) Isometric view of the micropillars, $\eta = 10$ μm.

Experimental section

Characterization of the micropillars

To evaluate the directional dependency, surfaces consisting of identical square micropillars with different values of spacing, D, and eccentricity, ε, were designed and subsequently fabricated on polydimethylsiloxane (PDMS) substrates. To reduce the amount of experimental data, the geometrical parameters of the pillars including the micropillar spacing and eccentricity were normalized with respect to the pillar pitch, $\lambda = L + D$. That is, $D^* = D/\lambda$ and $\varepsilon^* = \varepsilon/\lambda$, where D^* is the relative pillar spacing and ε^* is the normalized pillar eccentricity. The detailed geometrical parameters of the pillars are listed in Table 1.

Micropillar fabrication

PDMS micropillars were formed using a three-step double casting replication procedure. First, master mold micropillars were fabricated on silicon wafer using photolithography and deep reactive ion etching (DRIE) techniques.[35] In the second step, microhole structures were transferred on PDMS following a standard micromolding method.[37] Finally, micropillars were formed on another PDMS substrate using a double casting technique. To avoid irreversible bonding between two PDMS substrates, the surface of the PDMS microhole template was treated with trichloromethylsilane (TCMS, Sigma Aldrich) as the releasing agent[38] with the following procedure. First, oxygen plasma was used to render the PDMS microholes hydrophilic before the deposition of TCMS. Then, the PDMS slabs were

Table 1 Geometrical parameters of the fabricated PDMS square micropillars ($\eta = 10$ μm and $\lambda = 8$ μm)

L (μm)	D (μm)	ε (μm)	D^*	ε^*
6	2	0, 2, 4, 6	0.25	0, 0.25, 0.50, 0.75
5.3	2.7		0.33	

placed in a desiccator while 5 mL of TCMS was dripped in a Petri dish. The pressure of the chamber was reduced by pumping it for 90 minutes. Afterwards, the valve of the chamber connecting the pump was closed, and the pump was switched off. The total deposition process was conducted under a fume hood and the chamber was left overnight for the deposition to take place. After pouring another liquid PDMS on the TCMS-coated microhole substrate and solidifying it in an oven for 30 minutes at 85 °C, PDMS micropillars were successfully formed. The SEM images of these micropillar morphologies are shown in Fig. 1(a) and (b).

Contact angle measurement

An optical tensiometer (Theta Attension, BiolinScientific, Finland) was used to measure the contact angles and wettability conditions of the micropillar surfaces at the different viewing angles. The pixel error of the tensiometer is reported to be around 0.1 degrees.

Drop volume and deposition technique

The degree of anisotropic wetting could be affected by the size of the droplet.[27] We needed to compromise between a large and a small volume of the droplet. A large droplet volume is more stable but more prone to gravitational sagging. On the other hand, a small droplet volume is dominated by capillary pressure but evaporates quickly and may have a transient regime. Here, a water droplet of 2 μL was selected for the experiment. By denoting ρ and γ_w as the density and surface tension of water at room temperature, and r as the maximum droplet radius corresponding to the droplet volume of 2 μL, the Bond number is $Bo = \rho g r^2/\gamma_w = 0.08$. This value of the Bond number ensures that the influence of gravity is negligible compared to the surface tension. Having automatically pumped 2 μL volume of DI water from the delivery syringe, the drop was detached at the minimum distance between the tip of the needle and the surface. The drop was placed gently on the sample without compressing it to keep the spherical shape and to minimize the perturbation and kinematic pressure. After a minute, the image of the drop was captured and further analyzed using the built-in image analyzer of the tensiometer.

Methodology and statistical error

To evaluate the contact angle at each viewing direction systematically, each PMDS substrate consisting of four different micropatterned surfaces was attached to a rotary stage (Edmund Optics Inc.) along the y axis shown in Fig. 1(a). The corresponding angle on the rotary stage was fixed to 90° as the reference point. With the employed rotary stage, the sample can be rotated 360° with ±5° fine rotations.

Moreover, each measurement was repeated at least 6 times at different locations of the sample (at each specific D^*, ε^* and α) to ensure the repeatability of the data and the average value of the contact angle was found at 95% confidence interval. Corresponding statistical errors of the static contact angles were less than ±4°. Further error propagation and uncertainty analyses of the experimentally obtained parameters are presented in the Appendix.

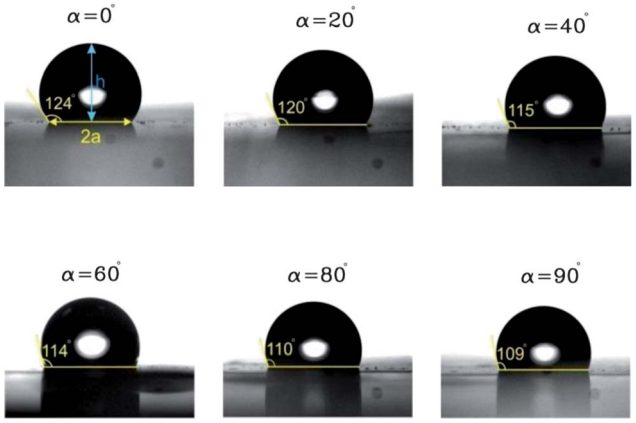

Fig. 2 Typical images of the contact angle anisotropy of the micropillar surfaces ($D^* = 0.25$ and $\varepsilon^* = 0.75$) of a single droplet by rotating the sample from (0–90°) in 20° step increments.

Fig. 2 depicts a typical measurement of contact angle anisotropy of a single droplet with counterclockwise (CCW) 90° rotation of the sample ($D^* = 0.25$ and $\varepsilon^* = 0.75$). This figure clearly shows the anisotropy of the fabricated surface, as the contact angle differs greatly at different viewing directions. Along the x-axis ($\alpha = 0°$) the contact angle is more than 124° and as the sample rotates CCW, it starts to decrease gradually, and the minimum occurs along the orthogonal direction with a contact angle of less than 109°.

Results and discussion

Raw experimental data

The average values of the contact angle on the micropillar surfaces of different D^* and ε^* as a function of viewing angles are shown in Fig. 3. In addition, the experimental values of the contact angle are also compared with the theoretical equation proposed by Cassie and Baxter, θ_{CB}:[39]

$$\cos\theta_{CB} = \phi_s \cos\theta_{smooth} + (1 - \phi_s)\cos\pi \quad (1)$$

where θ_{smooth} and π are contact angles on the smooth solid and gas portions, respectively, and ϕ_s is the solid area fraction of the micropillars. The contact angle on smooth PDMS was measured as $\theta_{smooth} = 109°$. The experimental contact angles on samples with zero eccentricities are in good agreement with the Cassie–Baxter equation. However, the results indicate that this equation can only predict the maximum achievable contact angle irrespective of the micropillar eccentricities.

Generally, the results show a periodicity trend for contact angle when the viewing angle gradually varies up to 180°. The period and amplitude (corresponding to the degree of contact angle anisotropy) of the samples are found to be a function of both micropillars normalized eccentricity and relative spacing. Most importantly, the amplitude is larger for the case of lower pillar spacing, where the degree of hydrophobicity is lower. This implies that contact angle anisotropy becomes more important as the hydrophobicity decreases. Specifically, the results indicate that even on micropillars with zero eccentricity, the contact angle is not isotropic. In this case, contact angles measured along the

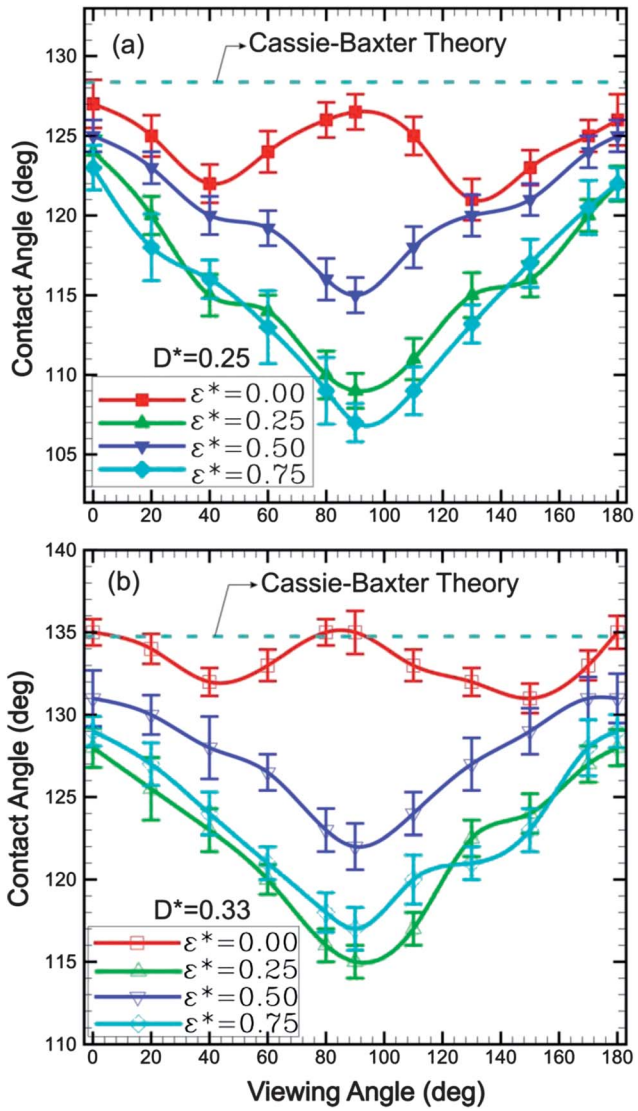

Fig. 3 Experimental contact angle θ *versus* viewing angle α at different values of normalized eccentricity ε^* and relative pillar spacing D^*. (a) $D^* = 0.25$. (b) $D^* = 0.33$.

sides of the pillars ($\alpha = 0°, 90°$) are the same but decrease as the viewing angle approaches the diagonal direction ($\alpha = 45°, 135°$). This is in qualitative agreement with the results reported by Neuhaus *et al.*,[34] and can be related to the different geometrical features. Thus, the droplet width at the three-phase contact line along the side is not equal to the one obtained along the diagonal direction. In that case, the droplet contact line deviates from the perfect circular shape.

By increasing the pillar normalized eccentricities to nonzero values, the period of the data increases to 180°. That means, for the pillars with nonzero eccentricities, the maximum contact angle occurs along the x-axis shown in Fig. 1(a). As the sample rotates, the contact angle decreases down to its minimum value along the perpendicular direction, *i.e.* y-axis in Fig. 1(a). Additionally, the results indicate that along a fixed viewing angle, the contact angle decreases by increasing the eccentricity, which is in good agreement with our results in a previous publication.[35]

Degree of anisotropic wetting

To further quantify the contact angle anisotropy, the degree of anisotropic wetting, δ, can be defined as:

$$\delta = \frac{\theta(\alpha)_{\max} - \theta(\alpha)_{\min}}{\theta(\alpha)_{\max} + \theta(\alpha)_{\min}} \times 100\% \quad (2)$$

where $\theta(\alpha)_{\max}$ and $\theta(\alpha)_{\min}$ are maximum and minimum contact angles on the same micropillar surface obtained at different viewing directions. According to the experimental data, the degree of anisotropic wetting δ can be found as a function of normalized eccentricity ε^* of the micropillars, Fig. 4.

The results suggest that the degree of anisotropic wetting of a surface can be tailored by changing both micropillar normalized eccentricity and relative spacing. As shown in Fig. 4, for the case of lower pillar relative spacing, increasing the pillar eccentricity also increases the degree of anisotropic wetting. This can be attributed to the increase in the anisotropic features of micropillars by increasing the eccentricity.

Moreover, Fig. 4 indicates that the degree of contact angle anisotropy decreases by increasing the relative pillar spacing. For instance, on the surface with $D^* = 0.25$ and $\varepsilon^* = 0.75$, the degree of anisotropic wetting is as high as 7% while it falls below 5% by increasing the relative spacing to 0.33. It was observed that as the relative pillar spacing increases, the degree of hydrophobicity also increases.[35] Therefore, the degree of contact angle anisotropy is inversely proportional to the degree of hydrophobicity. This result suggests that for anisotropic but highly hydrophobic micropatterned surfaces, directional dependency of the contact angle is less pronounced. This finding is also in agreement with the isotropic contact angle on the microstructures of a lotus leaf.[40]

Degree of anisotropic droplet distortion

In the present paper, at each viewing angle, the average drop width, $2a$, and the drop height, h, were measured from the

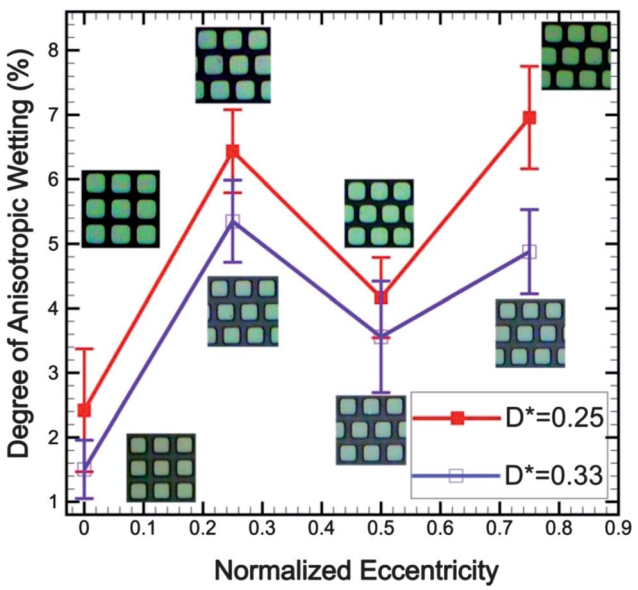

Fig. 4 Percentage of anisotropic wetting δ *versus* normalized eccentricity ε^* at different values of relative pillar spacing D^*.

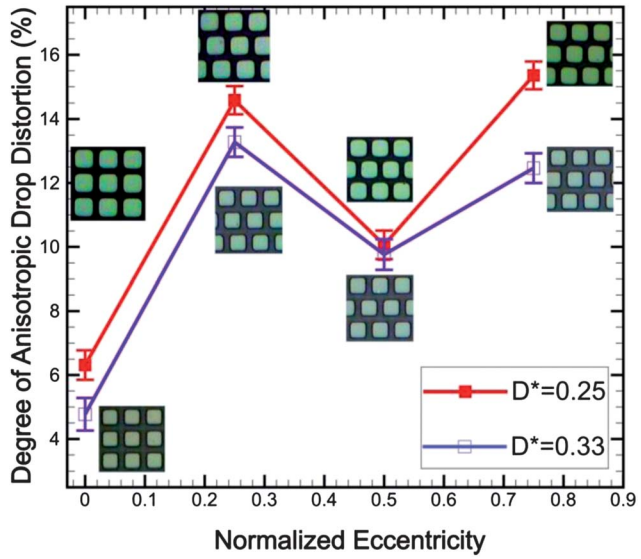

Fig. 5 Percentage of the degree of anisotropic droplet distortion ζ *versus* normalized eccentricity ε^* at different values of relative pillar spacing D^*.

recorded images of the droplet, with the bias error of ± 0.0005 mm, after proper calibration. Accordingly, the droplet aspect ratio, $a^* = a/h$, was determined. Subsequently, similar to the degree of wetting anisotropy, we can define the degree of the anisotropic droplet distortion ζ as follows:

$$\zeta = \frac{a^*(\alpha)_{\max} - a^*(\alpha)_{\min}}{a^*(\alpha)_{\max} + a^*(\alpha)_{\min}} \times 100\% \quad (3)$$

where $a^*(\alpha)_{\max}$ and $a^*(\alpha)_{\max}$ are the maximum and minimum droplet aspect ratios obtained at the different viewing angles α on the same micropillar surface.

The corresponding values of the degree of anisotropic droplet distortion ζ are plotted as a function of the normalized eccentricity ε^* in Fig. 5. The trend of increasing anisotropic drop distortion ζ is favored by decreasing the pillar relative spacing and increasing the pillar normalized eccentricity. This trend is consistent with the contact angle anisotropy, which confirms the accuracy of the measurements. The maximum anisotropic droplet distortion ζ occurs for the case of $D^* = 0.25$ and $\varepsilon^* = 0.75$ where $\zeta = 15\%$ leads to $\delta = 7\%$. Whereas for the case of $D^* = 0.33$ and $\varepsilon^* = 0$, anisotropic droplet distortion ζ is less than 5% and leads to an anisotropic wetting δ of 1.5%. This fact explains the reason why top-view macroscopic images of the drop placed on the micropillar surfaces with zero eccentricities represent a non-distorted, circular drop shape.

Furthermore, it should be noted that micropillars with $\varepsilon^* = 0.25, 0.75$ are mirror images of each other. Thus, the morphologies of the pillars are identical. Consistently, the results in Figs 4 and 5 confirm that the wetting anisotropy is similar on such surfaces, and droplets are elongated along the same mirror plane, *i.e.* y-axis in Fig. 1(a).

Three-phase contact line shape on anisotropic pillars

Owing to the existence of the roughness, the actual three-phase contact line of a droplet on rough surfaces is not smooth but rather corrugated which would give rise to the effect of contact line tension, an extra term in Gibbs free energy, as explained in our previous paper.[35] This micro/nanoscale corrugation may be very small, thus indistinguishable from smooth line macroscopically. For isotropic wetting/roughness, the shape of the contact line is assumed to be perfectly circular.[20] However, unequal droplet widths in contact with an isentropically rough surface are key parameters in directional dependency of the contact angle. If the degree of anisotropy is high, such as surfaces with hydrophilic and hydrophobic strips as well as groove structures, the elongation of the drop along a specific direction is macroscopically observable. Chen *et al.*[20] suggested an elliptical geometry as the equivalent noncircular smooth contact line shape for the case of parallel groove structures as supported by their experimental data and numerical simulation.

The values of the droplet aspect ratio a^* are plotted in Fig. 6 as a function of viewing angle α on a polar coordinate. To depict the

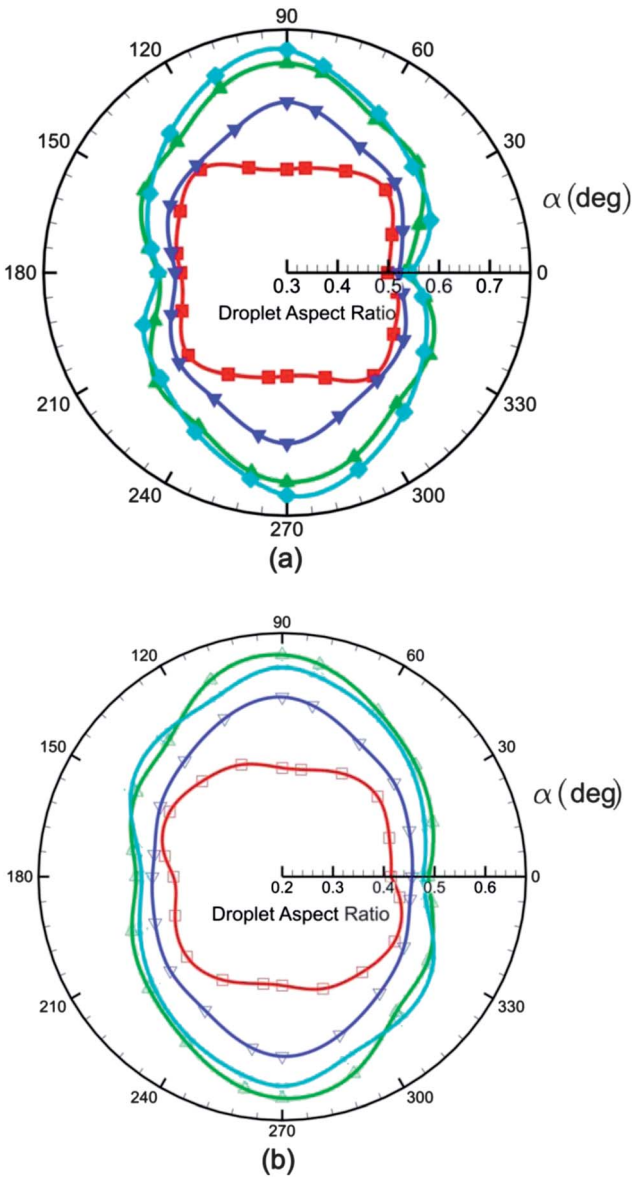

Fig. 6 Droplet aspect ratio a^* as a function of viewing angle α (°) on the polar coordinate. Spline interpolation between the experimental date represents the three-phase contact line of the droplet (a) $D^* = 0.25$; (b) $D^* = 0.33$ (line legend is the same as that of Fig. 3).

contact line shape of the droplet, spline interpolation is used to fit these experimental data. It should be noted that the values of the aspect ratio for $\alpha = 180$–360° are found based on the symmetrical conditions of the microstructures, *i.e.* the obtained curves from $\alpha = 0$–180° are mirrored with respect to the horizontal line. Fig. 6 clearly illustrates the corrugation of the three-phase contact line of the microstructured surfaces and its corresponding shapes by increasing the pillar eccentricity as well as the relative spacing. The result also illustrates that the variations of the contact line shape are more pronounced by changing the micropillar eccentricities. That means wetting anisotropy is highly affected by the micropillar eccentricity, rather than relative spacing, as confirmed by the experimental contact angles shown in Fig. 3.

Semi-analytical model to predict 3D droplet shape on an anisotropic surface

To obtain the equilibrium drop shape on any surface, the Gibbs free energy of the surface should be minimized subject to some constraints such as constant drop volume conditions forming the basis of numerical tools such as the Surface Evolver software.[41] However, for microstructured surfaces where the size of the droplet is much larger than the characteristic length of the patterns, it was shown that finding the equilibrium drop shape is extremely difficult due to the computational complexity of the problem.[20] Another alternative approach to find the equilibrium drop shape is to solve the nonlinear partial differential equation of the Young–Laplace equation developed for the sessile drop. It can be proven mathematically that if the Bond number is less than unity, and the characteristic length of the drop is less than the capillary length δ_c of the liquid, the shape of the drop becomes spherical cap which is the solution of the Young–Laplace equation by neglecting the hydrostatic pressure. Such an axisymmetric drop placed on a hydrophobic surface is illustrated in Fig. 7.

For an anisotropic surface at each viewing angle α the value of the contact angle θ is different. Thus, the contact angle can be expressed as a function of α, $\theta = f(\alpha)$.

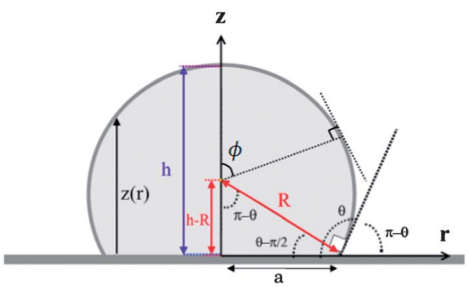

Fig. 7 Axisymmetric drop shape on a hydrophobic surface.

Using the current experimental data in Fig. 3, $f(\alpha)$ can be approximated as a Fourier series (with periods $T = \pi$ for nonzero eccentricities and $T = \pi/2$ for zero eccentricities) as follows.

$$\theta = f(\alpha) = a_0 + \sum_{n=1}^{\infty} a_n \cos\frac{2n\pi}{T}\alpha \approx a_0 + a_1 \cos\frac{2\pi}{T}\alpha + a_2 \cos\frac{4\pi}{T}\alpha \quad (4)$$

where the cosine Fourier series up to the first two sums are used for curve-fitting of the measured data. The values of a_0, a_1, and a_2 are listed in Table 2 for each micropillar surface.

Using the geometrical relations as well as the fact that the height of the drop h is constant at any viewing angle α, the 2D form of the drop becomes:

$$r(\phi) = \frac{h}{(1-\cos\theta)}\sin\phi \quad (5\text{-a})$$

$$z(\phi) = h - \frac{h}{(1-\cos\theta)}(1-\cos\phi) \quad (5\text{-b})$$

where ϕ is the zenith angle, as shown in Fig. 7. For an anisotropic surface at different viewing angles α, the values of the contact angle θ are different. This continuous function was obtained using eqn (4). Therefore, the final 3D form of the equilibrium droplet shape on anisotropic surfaces becomes:

$$x^* = \frac{\sin\phi}{1-\cos(f(\alpha))}\cos\alpha \quad (6\text{-a})$$

$$y^* = \frac{\sin\phi}{1-\cos(f(\alpha))}\sin\alpha \quad (6\text{-b})$$

$$z^* = 1 - \frac{1-\cos\phi}{1-\cos(f(\alpha))} \quad (6\text{-c})$$

where $0 \le \phi \le \theta$, $0 \le \alpha \le 2\pi$, and $x^* = x/h$; $y^* = y/h$; $z^* = z/h$.

Finally, by varying α from 0 to 360°, the 3D shape of the drop can be plotted. These shapes at different values of pillar relative spacing and eccentricity are presented in Fig. 8(a)–(h). The results shown in Fig. 8 confirmed our previous discussions regarding the degrees of anisotropic wetting and droplet distortion by changing the micropillars eccentricity and relative spacing. As illustrated in Fig. 8, increasing the relative pillar spacing D^* as well as decreasing the pillar normalized eccentricity ε^* make the droplet shape closer to the symmetrical configuration. If the geometric parameters of the micropillars are tailored such that the anisotropic wetting increases, it can be concluded that the energy barriers of the surface also increase as compared to the isotropic features and wettability increases. This

Table 2 Coefficients of the Fourier series, eqn (4), for the micropillars used in this study

	$D^* = 0.25$				$D^* = 0.33$			
	$\varepsilon^* = 0$	$\varepsilon^* = 0.25$	$\varepsilon^* = 0.50$	$\varepsilon^* = 0.75$	$\varepsilon^* = 0$	$\varepsilon^* = 0.25$	$\varepsilon^* = 0.50$	$\varepsilon^* = 0.75$
a_0	2.168	2.017	2.098	2.001	2.330	2.128	2.220	2.144
a_1	0.043	0.106	0.071	0.118	0.024	0.102	0.0719	0.091
a_2	0.000	0.012	0.001	0.000	0.001	−0.009	−0.009	0.009

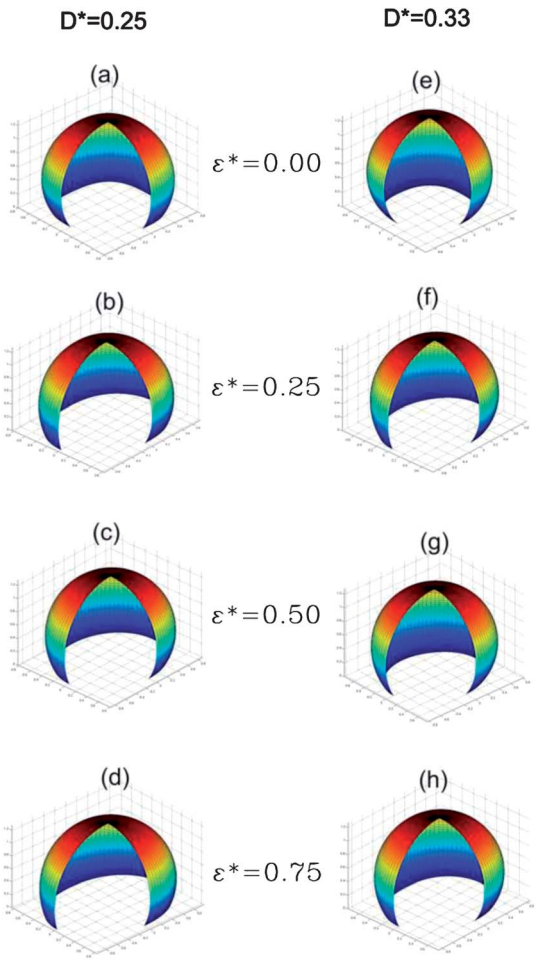

Fig. 8 Three-quarters of an equilibrium drop shape with $V = 2$ μL. From top to bottom, the effects of increasing the pillars eccentricity are shown, *i.e.* (a–d) and (e–h), while from left to right, the effects of increasing the pillars relative spacing are illustrated, *e.g.* (a and e) or (d and h).

is in excellent agreement with the thermodynamic model presented by Zhao *et al.*[23] derived by calculating the wetting surface energy of the system as the contact line moves along two orthogonal directions for parallel groove structures.

For the case of discrete micropillars, the obtained results can be explained by taking into consideration the corrugation of the three-phase contact line which is the main reason for the directional dependency of the contact angle. The distorted nature of the three-phase contact line, as illustrated in Fig. 6, as well as the corrugated drop shapes found from the simulated results (Fig. 8) by increasing anisotropic wetting, increases the value of the line tension term of Gibbs free energy, *i.e.* the energy required to change the length of the three-phase contact line.

As explained in our previous paper,[35] the importance of the line tension becomes more pronounced when the contact line is corrugated. The corrugation gives rise to the energy barrier of the system, and hence decreases the degree of hydrophobicity. For the case of zero eccentricity, *i.e.*, Fig. 8(a) and (e), the energy barrier is larger on the diagonal direction of the pillars, and as a result, the contact line would be distorted as shown in Fig. 6. Distortion of the contact line along the diagonal direction causes unequal drop widths and leads to contact angle anisotropy. On the surfaces with nonzero eccentricities, line tension, equivalent to the energy barrier and contact line distortion, increases along $\alpha = 90^\circ$ (y-axis in Fig. 1(a)). Likewise, as the sample rotates toward the features along the x-axis (orthogonal direction) the energy barrier decreases, and the contact line corrugation becomes smaller and closer to the circular shape.

Conclusions

This paper experimentally investigated the anisotropic wetting of surfaces patterned with discrete micropillars. Square micropillars with different values of relative spacing D^* as well as normalized eccentricity ε^* were fabricated using double casting PDMS replica molding. Contact angles were measured by gradually rotating the sample at different viewing angles α. The contact angle anisotropy was found to be a periodic function of the viewing angle whose period was $\pi/2$ and π for zero and nonzero values of eccentricity, respectively. To quantify the directional dependency of the contact angle on such geometries, both degrees of anisotropic wetting δ and droplet distortion ζ were defined. It was observed that both δ and ζ increased by increasing the pillar eccentricity as well as decreasing the pillar relative spacing. However, the effect of changing the pillar eccentricity was much more pronounced. On the surface with $D^* = 0.33$ and $\varepsilon^* = 0$, minimum anisotropy was observed, *i.e.* $\delta_{min} = 1.5\%$ and $\zeta_{min} = 4.8\%$. By decreasing the relative pillar spacing to 0.25 and increasing the normalized eccentricity to 0.75, maximum anisotropy was observed, *i.e.* $\delta_{max} = 7\%$ and $\zeta_{max} = 15\%$. Also, on the patterns which were mirror images of each other, $\varepsilon^* = 0.25$ and $\varepsilon^* = 0.75$, the contact angle anisotropy was consistently identical. Additionally, by measuring the droplet aspect ratio a^* at each viewing angle, the three-phase contact line shape of the water droplet at each D^* and ε^* was found (2D approach). The three-phase contact line shapes on discrete anisotropic micropillars were highly corrugated at the microscopic scale. This fact explains why macroscopic images of the drop placed on the micropillar surfaces with zero eccentricities represent a non-distorted, circular drop shape. Furthermore, a semi-analytical model based on a low Bond number was developed to describe the equilibrium 3D shape of the droplet (3D approach). The model is strictly based on the relationship between the droplet contact angle θ and the viewing angle α. This relationship was approximated by curve fitting of the experimental data using Fourier series. Based on the model, equilibrium 3D shapes of the droplet at different D^* and ε^* were found, and a good qualitative agreement was obtained with the experimental results. Both of these 2D and/or 3D approaches are extremely useful to detect the corrugated shapes of the three-phase contact line. Generally, it was found that both wetting anisotropy of the micropillars and the degree of the hydrophobicity of the surface have the same trend and are interrelated. That means, by increasing micropillar normalized eccentricity, the energy barriers (fluctuations in the free energy) of the system also increase. This gives rise to the distortion of the three-phase contact line. The corrugation of the contact line is the main source of anisotropy. The results also showed that the energy barrier of the micropillar structures with nonzero eccentricities increases gradually in the orthogonal direction with a period of 180°, whereas for micropillars with zero eccentricities, it has a period of 90°. Finally, the results of

the current paper suggested that combined effects of pillar relative spacing, normalized eccentricity, and viewing angle should be taken into consideration when evaluating the contact angle anisotropy and wetting conditions of the microstructured surfaces.

Appendix: uncertainty and error propagation of the experimental data

Generally, if z is a function of independent variables x and y, $z = f(x,y)$, the uncertainty of z, Δu_z, becomes:

$$\Delta u_z = \sqrt{\left(\frac{\partial f}{\partial x}\Delta u_x\right)^2 + \left(\frac{\partial f}{\partial y}\Delta u_y\right)^2} \quad \text{(A1)}$$

where Δu_x and Δu_y are uncertainties of x and y, respectively. For $z = (x - y)/(x + y)$, it becomes:

$$\frac{\partial f}{\partial x} = \frac{2y}{(x+y)^2}\,;\ \frac{\partial f}{\partial y} = \frac{-2x}{(x+y)^2} \quad \text{(A2)}$$

Substituting eqn (A2) in eqn (A1) results in:

$$\Delta u_z = \frac{2}{(x+y)^2}\sqrt{y^2\,\Delta u_x{}^2 + x^2\,\Delta u_y{}^2} \quad \text{(A3)}$$

This formula is used to calculate the uncertainties of δ by replacing $x \rightarrow \theta(\alpha)_{\max}$ and $y \rightarrow \theta(\alpha)_{\min}$ and are shown by error bars in Fig. 4.

Similarly, the error propagation of ζ can be calculated by replacing $x \rightarrow a^*(\alpha)_{\max}$ and $y \rightarrow a^*(\alpha)_{\min}$ in eqn (A3). To find the uncertainty of the maximum/minimum droplet aspect ratio, $\Delta u_{a^*\max/\min}$, one can write:

$$\Delta u_{a^*\max/\min} = \sqrt{\left(\frac{\Delta u_a}{h}\right)^2 + \left(\frac{-a}{h^2}\Delta u_h\right)^2} = \frac{\Delta u_a}{h}\sqrt{1 + a^{*2}} \quad \text{(A4)}$$

where the uncertainties in a and h are calculated from:

$$\Delta u_h = \Delta u_a = 2\sqrt{e_b{}^2 + \left(\frac{e_s}{\sqrt{N}}\right)^2} \quad \text{(A5)}$$

In eqn (A5), e_b is the bias error as a result of the limited accuracy of measuring a and h, $e_b = 0.0005$ mm, and e_s is the systematic error due to deviation of the measured volume from the desired volume (2 μL), and N is the number of the samples.

These uncertainties of ζ are represented by error bars in Fig. 5.

Notes and references

1 L. Feng, S. Li, Y. Li, H. Li, L. Zhang, J. Zhai, Y. Song, B. Liu, L. Jiang and D. Zhu, *Adv. Mater.*, 2002, **14**, 1857–1860.
2 T. Sun, L. Feng, X. Gao and L. Jiang, *Acc. Chem. Res.*, 2005, **38**, 644–652.
3 H. Wu, R. Zhang, Y. Sun, D. Lin, Z. Sun, W. Pan and P. Downs, *Soft Matter*, 2008, **4**, 2429–2433.
4 Y. Zheng, X. Gao and L. Jiang, *Soft Matter*, 2007, **3**, 178–182.
5 A. Neumann and R. Good, *J. Colloid Interface Sci.*, 1972, **38**, 341–358.
6 H. Gau, S. Herminghaus, P. Lenz and R. Lipowsky, *Science*, 1999, **283**, 46–49.
7 S. Brandon, N. Haimovich, E. Yeger and A. Marmur, *J. Colloid Interface Sci.*, 2003, **263**, 237–243.
8 M. Morita, T. Koga, H. Otsuka and A. Takahara, *Langmuir*, 2005, **21**, 911–918.
9 O. Bliznyuk, E. Vereshchagina, E. S. Kooij and B. Poelsema, *Phys. Rev. E: Stat., Nonlinear, Soft Matter Phys.*, 2009, **79**, 041601–041606.
10 H. P. Jansen, O. Bliznyuk, E. S. Kooij, B. Poelsema and H. J. W. Zandvliet, *Langmuir*, 2011, **28**, 499–505.
11 E. Kooij, H. Jansen, O. Bliznyuk, B. Poelsema and H. Zandvliet, *Colloids Surf., A*, 2012, **413**, 328–333.
12 D. Zhu, X. Li, G. Zhang, X. Zhang, X. Zhang, T. Wang and B. Yang, *Langmuir*, 2010, **26**, 14276–14283.
13 X. Zhang, Y. Cai and Y. Mi, *Langmuir*, 2011, **27**, 9630–9637.
14 J. Y. Chung, J. P. Youngblood and C. M. Stafford, *Soft Matter*, 2007, **3**, 1163–1169.
15 C. Bukowsky, J. M. Torres and B. D. Vogt, *J. Colloid Interface Sci.*, 2011, **354**, 825–831.
16 A. Buguin, L. Talini and P. Silberzan, *Appl. Phys. A: Mater. Sci. Process.*, 2002, **75**, 207–212.
17 T. Wang, X. Li, J. Zhang, X. Wang, X. Zhang, X. Zhang, D. Zhu, Y. Hao, Z. Ren and B. Yang, *Langmuir*, 2010, **26**, 13715–13721.
18 T.-i. Kim and K. Y. Suh, *Soft Matter*, 2009, **5**, 4131–4135.
19 H. Schonhorn, *J. Adhes.*, 1987, **23**, 147–161.
20 Y. Chen, B. He, J. Lee and N. A. Patankar, *J. Colloid Interface Sci.*, 2005, **281**, 458–464.
21 A. D. Sommers and A. M. Jacobi, *J. Micromech. Microeng.*, 2006, **16**, 1571–1578.
22 F. Zhang and H. Y. Low, *Langmuir*, 2007, **23**, 7793–7798.
23 Y. Zhao, Q. Lu, M. Li and X. Li, *Langmuir*, 2007, **23**, 6212–6217.
24 A. Sommers and A. Jacobi, *J. Colloid Interface Sci.*, 2008, **328**, 402–411.
25 H. Kusumaatmaja, R. J. Vrancken, C. W. M. Bastiaansen and J. M. Yeomans, *Langmuir*, 2008, **24**, 7299–7308.
26 W. Li, G. Fang, Y. Li and G. Qiao, *J. Phys. Chem. B*, 2008, **112**, 7234–7243.
27 J. Yang, F. R. A. J. Rose, N. Gadegaard and M. R. Alexander, *Langmuir*, 2009, **25**, 2567–2571.
28 L. Liu, A. M. Jacobi and D. Chvedov, *J. Micromech. Microeng.*, 2009, **19**, 035026–035034.
29 C. J. Long, J. F. Schumacher and A. B. Brennan, *Langmuir*, 2009, **25**, 12982–12989.
30 X. Yong and L. T. Zhang, *Langmuir*, 2009, **25**, 5045–5053.
31 W. Choi, A. Tuteja, J. M. Mabry, R. E. Cohen and G. H. McKinley, *J. Colloid Interface Sci.*, 2009, **339**, 208–216.
32 D. Xia, X. He, Y. B. Jiang, G. P. Lopez and S. Brueck, *Langmuir*, 2010, **26**, 2700–2706.
33 D. Wu, Q. D. Chen, J. Yao, Y. C. Guan, J. N. Wang, L. G. Niu, H. H. Fang and H. B. Sun, *Appl. Phys. Lett.*, 2010, **96**, 053704–053706.
34 S. Neuhaus, N. D. Spencer and C. Padeste, *ACS Appl. Mater. Interfaces*, 2011, **4**, 123–130.
35 N. Kashaninejad, W. K. Chan and N.-T. Nguyen, *Langmuir*, 2012, **28**, 4793–4799.
36 D. Öner and T. J. McCarthy, *Langmuir*, 2000, **16**, 7777–7782.
37 N. Kashaninejad, N.-T. Nguyen and W. K. Chan, *Phys. Fluids*, 2012, in press.
38 M. Sun, C. Luo, L. Xu, H. Ji, Q. Ouyang, D. Yu and Y. Chen, *Langmuir*, 2005, **21**, 8978–8981.
39 A. Cassie and S. Baxter, *Trans. Faraday Soc.*, 1944, **40**, 546–551.
40 D. Quéré, *Annu. Rev. Mater. Res.*, 2008, **38**, 71–99.
41 K. A. Brakke, *Experimental Mathematics*, 1992, **1**, 141–165.

